nature microbiology

ARTICLES

https://doi.org/10.1038/s41564-019-0369-x

Atomic structure of the translation regulatory protein NS1 of bluetongue virus

Adeline Kerviel[1,5], Peng Ge[2,5], Mason Lai[2,3,5], Jonathan Jih[2], Mark Boyce[1], Xing Zhang[2,4], Z. Hong Zhou[2,3*] and Polly Roy[1*]

Bluetongue virus (BTV) non-structural protein 1 (NS1) regulates viral protein synthesis and exists as tubular and non-tubular forms in infected cells, but how tubules assemble and how protein synthesis is regulated are unknown. Here, we report near-atomic resolution structures of two NS1 tubular forms determined by cryo-electron microscopy. The two tubular forms are different helical assemblies of the same NS1 monomer, consisting of an amino-terminal foot, a head and body domains connected to an extended carboxy-terminal arm, which wraps atop the head domain of another NS1 subunit through hydrophobic interactions. Deletion of the C terminus prevents tubule formation but not viral replication, suggesting an active non-tubular form. Two zinc-finger-like motifs are present in each NS1 monomer, and tubules are disrupted by divalent cation chelation and restored by cation addition, including Zn^{2+}, suggesting a regulatory role of divalent cations in tubule formation. In vitro luciferase assays show that the NS1 non-tubular form upregulates BTV mRNA translation, whereas zinc-finger disruption decreases viral mRNA translation, tubule formation and virus replication, confirming a functional role for the zinc-fingers. Thus, the non-tubular form of NS1 is sufficient for viral protein synthesis and infectious virus replication, and the regulatory mechanism involved operates through divalent cation-dependent conversion between the non-tubular and tubular forms.

Viruses commonly hijack cellular translational machineries to synthesize viral proteins from their mRNAs using diverse strategies[1]. In addition, some viruses, exemplified by members of the *Reoviridae* family, also enhance their gene expression using virally encoded proteins[1–4]. Among them, rotaviruses and orbiviruses (for example, bluetongue virus (BTV)) use non-structural proteins for this purpose. Similar to cellular mRNAs, the 5′ termini of mRNAs of these viruses are capped by viral-encoded structural proteins. However, unlike cellular mRNAs and most eukaryotic viruses, the 3′ termini of these viral mRNAs lack a poly(A) tail, which is responsible for enhancing the rate of translation initiation and the stability of RNA. Thus, to specifically upregulate protein synthesis from viral mRNA, viral proteins must bind to viral mRNAs selectively over poly(A)-tailed cellular mRNAs. To accomplish this, BTV uses a viral-encoded protein, non-structural protein 1 (NS1), a 64-kDa protein, which does not bind to any poly(A)-tailed mRNA, but has specific binding affinity for the 3′ terminal sequences of BTV mRNAs to upregulate viral protein synthesis[4]. In rotavirus, the non-structural viral protein NSP3 substitutes the cellular poly(A)-binding protein and binds to the viral mRNAs via 3′ terminal sequences[2]. Although biochemical studies and structural studies of NSP3 fragments have yielded some understanding about how this protein may enhance viral mRNA synthesis, high-resolution structures for full-length rotavirus NSP3 and BTV NS1, as well as a detailed molecular understanding of how these viral proteins function, are still lacking[3,5–8].

BTV is transmitted by biting midges of the *Culicoides* genus to ruminants, and is endemic worldwide. BTV infection in sheep and cattle often causes high morbidity and mortality with substantial economic consequences. The BTV genome consists of 10 segments (S1–S10) of double-stranded RNA, which encode seven structural proteins and four non-structural proteins (NS1–NS4). NS1 is an early protein expressed in infected host cells at a high level. Within the host cytoplasm, multiple copies of NS1 rapidly assemble in tubular form, a hallmark of orbivirus infections. NS1 tubules can either be purified from BTV-infected cells or assembled from recombinant proteins[9,10] for structural determination by cryo-electron microscopy (cryoEM) with helical reconstruction. A low-resolution (40 Å) three-dimensional (3D) reconstruction of NS1 tubules generated by recombinant NS1, was previously reported in 1992 (ref. [9]). However, owing to technical limitations, efforts to sort out multiple helical forms to improve the resolution of NS1 helical reconstruction have been unsuccessful for the past three decades. As such, how NS1 assembles into helical tubules and how such assemblies participate in BTV gene expression remain unclear.

Here, we report the near-atomic resolution structures of two NS1 tubular forms obtained by cryoEM. The atomic model shows that each NS1 monomer contains two metal binding, zinc-finger-like motifs and an extended carboxy-terminal arm, which interacts with neighbouring subunits to form tubules with variable diameters and helical configurations. The structure rationalizes many of the previous observations attributed to NS1 and suggests how tubules may form from a soluble pool of functional intermediates through coordination of zinc or other metal cations. Furthermore, structure-based mutagenesis of NS1, combined with reverse genetics, allowed us to determine that the non-tubular form of NS1 is also functional and to identify the critical residues involved in viral protein translation and replication, which may be shared by other members of the orbivirus family.

Results

Structure determination of NS1 tubules and atomic modelling. A challenge in the structural study of the BTV NS1 protein is its

[1]Department of Pathogen Molecular Biology, London School of Hygiene and Tropical Medicine, London, UK. [2]California NanoSystems Institute, University of California, Los Angeles (UCLA), Los Angeles, CA, USA. [3]Department of Microbiology, Immunology & Molecular Genetics, UCLA, Los Angeles, CA, USA. [4]Center of Cryo Electron Microscopy, Department of Biophysics, Zhejiang University School of Medicine, Hangzhou, China. [5]These authors contributed equally: Adeline Kerviel, Peng Ge, Mason Lai. *e-mail: Hong.Zhou@UCLA.edu; Polly.Roy@lshtm.ac.uk

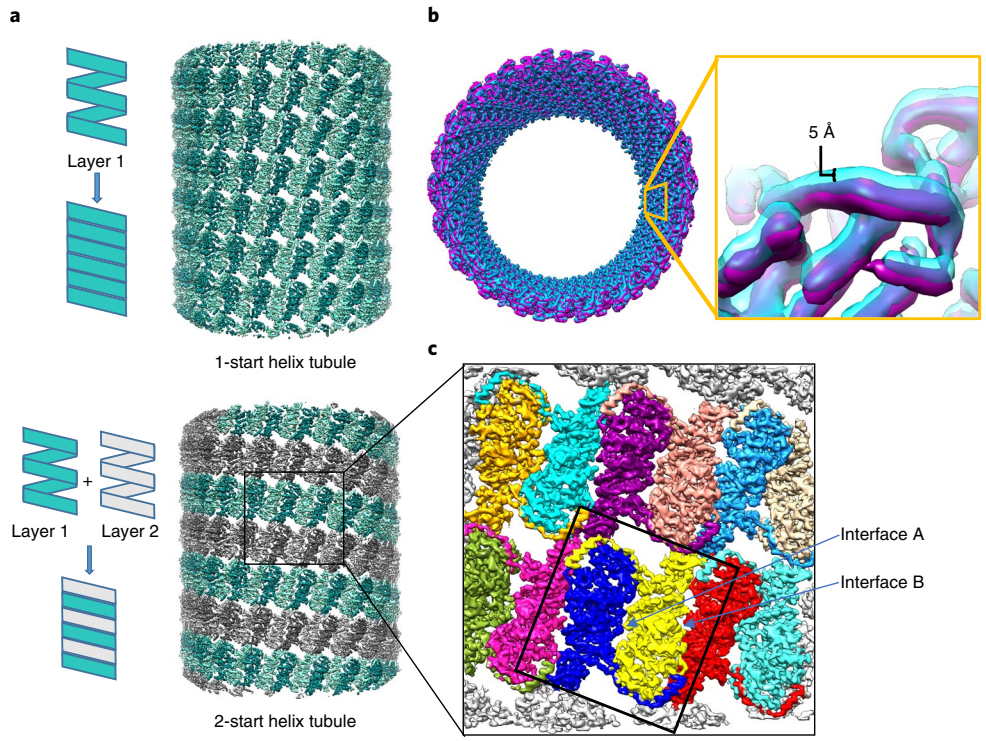

Fig. 1 | NS1 tubules are dynamic. a, Schematic (left) and reconstructions (right) of a 2-start NS1 tubule and a 1-start NS1 tubule. **b**, Overlaid surface view of the density maps of the largest diameter class (magenta) and smallest diameter class (blue). Note the colour dominance of the small diameter class along the inside of the tubule, illustrating its smaller diameter. **c**, Zoomed-in view of a region of the cryoEM density map of the NS1 tubule at 4.0 Å. Individual monomers are coloured differently to distinguish the borders of interacting monomers. Monomer–monomer interfaces A and B are indicated.

variable tubular forms as recognized nearly 30 years ago[9]. Such variability makes indexing of the helical parameters difficult and has hitherto prevented achieving high-resolution 3D structures. As technology availed, here, we have improved the resolution of the structure (see details in Methods) and determined the multiple helical configurations of the tubules based on our film data, but were unable to reach a resolution that is sufficient for atomic modelling. NS1 tubules vary in two major helical settings: subunits per turn (19.xx, 20.xx, 21.xx, 22.xx; where xx means not fixed) and helical start number (1–3 helices). The diameter of the tubule increases as the integer part of the subunits per turn number increases, ranging from 500 Å to 523 Å, 547 Å, 580 Å for 19.2, 20.2, 21.2 and 22.2 subunits per turn, respectively. The single (1-start) helices are always $y+1/5$ (y in [19.22]) subunits per turn, 2-start $y+4/7$ subunits per turn and 3-start $y+1$ subunits per turn. Thus, we observed, by combination, 12 (4×3) different helical forms, although we do not rule out the existence of other forms of undetectable populations.

We focused on the two most abundant classes of tubules with the following helical configurations: 20.2 subunits per turn, 1-start helical tubule (17.5%) and 20.58 subunits per turn, 2-start helical tubule (26.8%) (Fig. 1a). The tubule diameter increases from ~523 Å in the 1-start tubule to ~526 Å in the 2-start tubule. The tubules that belong to the same helical configuration appear to 'breathe' due to thermal motions—for four different classes of 3D classification, the radii of 20.58 tubules vary by up to ~5 Å (Fig. 1b). Such variability has necessitated exhaustive computational classification to reduce the number of particles in each homogeneous structural class. Thus, although a meaningful signal can be recognized to 3.8 Å in the power spectrum of electron-counting cryoEM images, the resolution of the 3D reconstruction (Fig. 1c) from best class, obtained by merging 4,517 particles, is limited to ~4.0 Å, as judged from the structural features (Fig. 2a) and Fourier shell correlation analysis (Supplementary Fig. 1).

Structure reveals that the 2-start helical tubule is formed by pseudo-planar NS1 homodimers arranged into a thin-walled (~57 Å) tubule, containing 41.16 monomers per turn. Its architecture is stabilized laterally by packing interactions between neighbouring NS1 subunits of the same layer, and vertically by compact junctions between six monomers from two different layers (Fig. 1c). This helical arrangement differs from that reported previously[9]. Remarkably, the 1-start/2-start helical change in the tubule arrangement does not alter the monomeric structure in a noticeable manner, reminiscent of the formation of a carbon nanotube from graphene[11]. NS1 monomers interact with its neighbours through two interfaces: A and B (Fig. 1c). The dimers are packed together in the 1-start in an upright position with respect to the tubule axis (the angle between the dimer interface and the tubule axis is 18.8° and 20.7° in the 1-start and 2-start tubules, respectively). There are no major changes in subunit–subunit interactions between the two helical forms, and only a subtle shift in the arrangement of each subunit with its neighbours. These similarities and differences indicate an assembly mechanism of an NS1 tubule from a flat and flexible sheet, a process that allows different helical configuration to form.

Structure of the NS1 monomer. NS1 has no known structural homologues, and its repeating arrangement with entwined extensions in the tubule created difficulties in de novo modelling. Some prominent structural features, such as aromatic side chains (Fig. 2a), and the visible C terminus provided key landmarks for model building. Subsequently, integration of a structural map with sequence-based prediction and available functional data allowed us to complete a provisional model consisting of two of the three globular domains of the NS1 monomer. In retrospect, resolving key junctions at domain boundaries was challenging due to confusion caused by the previously unknown presence of metal ion coordination

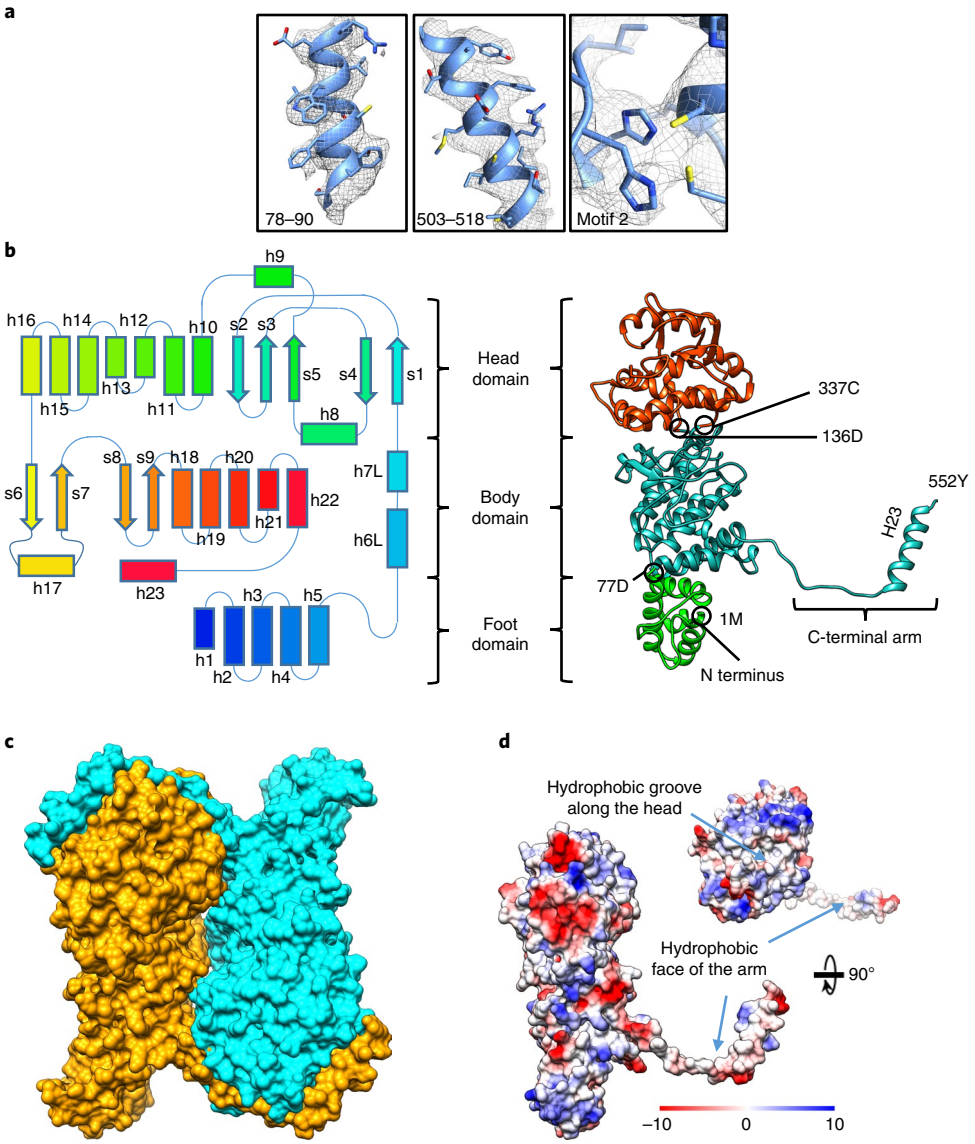

Fig. 2 | Structure of the NS1 monomer. a, Superposition of the cryoEM densities (grey mesh) and their corresponding atomic models (ribbon and sticks) for three selected regions of NS1, illustrating the quality of the cryoEM densities that supports atomic modelling based on amino acid side chains. **b**, Secondary structure schematic and domain architecture (left) mapped to the atomic model (shown as a ribbon diagram to the right) of an NS1 monomer. **c**, Space-filling surface rendering of an NS1 dimeric building subunit of both tubular forms. **d**, Coulombic surface rendering of the NS1 monomer showing the C-terminal arm handshake. Note the hydrophobic groove in the head domain and the hydrophobic inner surface of the C-terminal arm. Surface colouring is based on the residue charge properties (red, negative; blue, positive).

motifs. Such motifs created density branches that obscure chain tracing. Once these two globular domains were assigned, the remaining globular domain and the C-terminal arm became readily assignable to the correct monomer, allowing de novo modelling and refinement of the first NS1 atomic model (Fig. 2b).

Each NS1 monomer is organized into three domains (Fig. 2b): foot, body and head, with the amino terminus located in the foot domain and the C terminus extending far from the body domain through an 'arm'. Monomers are arranged in the tubule in an alternating head-to-foot orientation (Fig. 2c). The head domain consists of nine α-helices and two β-sheets. One of the β-sheets contains anti-parallel strands and the other, both anti-parallel and parallel strands. The body domain lies between the head domain and the foot domain. It comprises two β-sheets and six α-helices. The foot domain (residues 1–77) is composed of five α-helices, with two linker helices, h6L and h7L, traversing the body domain to reach the head domain (residues 136–337).

The C-terminal arm is necessary for tubule formation but not for virus replication. The NS1 C-terminal arm contains a 15-residue long α-helix (h23, residues 535–550) and connects to the globular body domain through helix 22 upstream (Fig. 2b). The hydrophobic arm extends from the body and occupies a hydrophobic groove on the neighbouring monomer, whereas its terminal helix displays a hydrophobic face to grasp the head domain of the neighbouring monomer (Fig. 2c,d). Each monomer reaches out to join the neighbouring monomer and, in turn, is inter-linked by its partner (Fig. 2c). Furthermore, the hydrophobic β-strand section (residues 522–526) of the C-terminal arm augments a β-sheet in the head domain of the neighbouring monomer formed by strands s2, s3 and s5 (Fig. 3a).

Previous biochemical studies[12] have shown that the C-terminal 10 amino acids are essential for tubule formation, suggesting that the C-terminal helix is involved in tubule formation. To investigate this, two C-terminal deletion mutants, Δ20 (Δ532–552) and

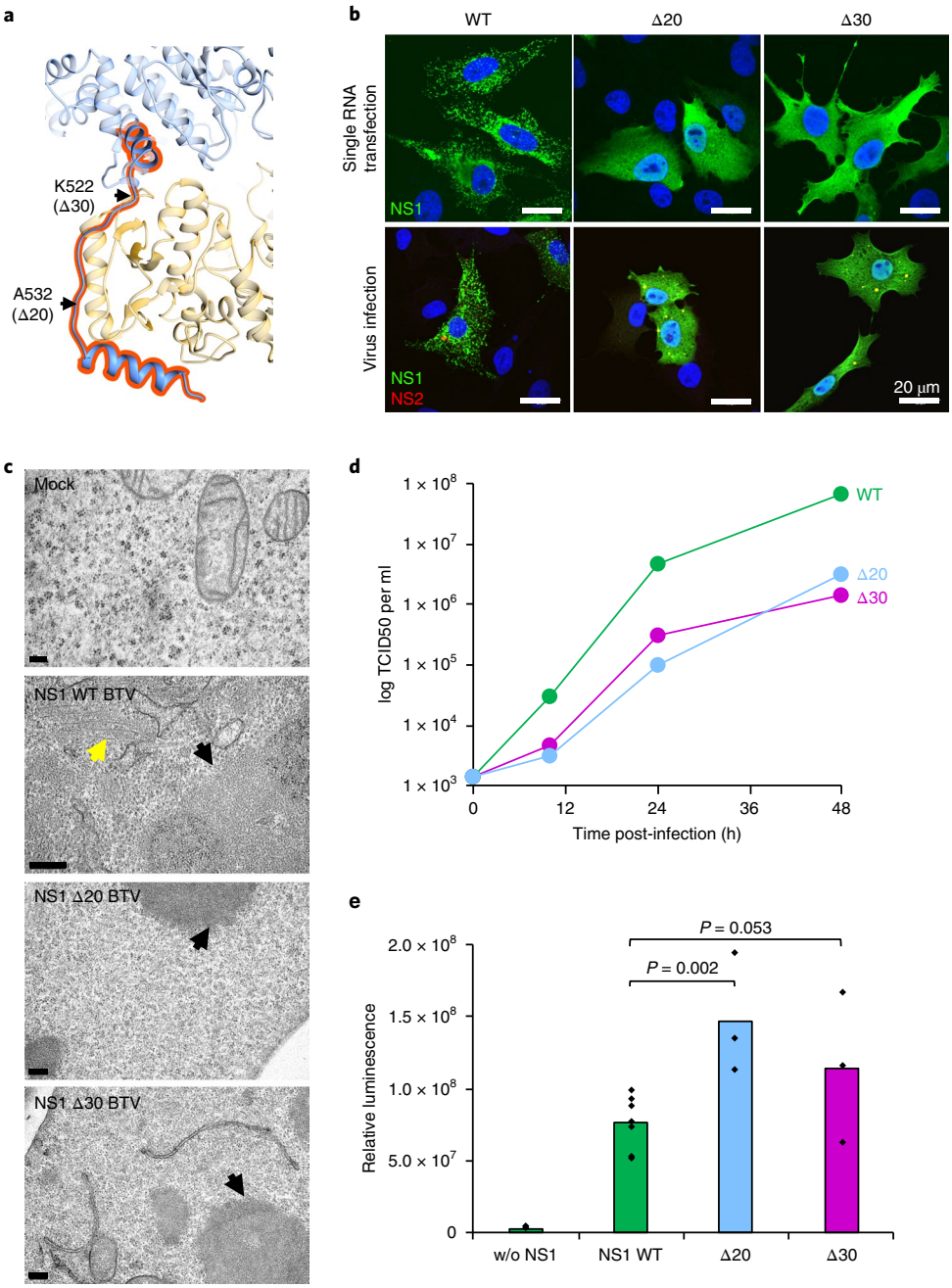

Fig. 3 | C-terminal arm deletion mutations demonstrate that the non-tubular form of NS1 is the functional form. a, Ribbon diagram inter-NS1 interface showing the locations of the two C-terminal arm deletion mutants. The β-sheet augmentation and handshake grip region of the C-terminal arm are highlighted in red. Residues for the deletion mutants are labelled. **b**, Immunofluorescence analysis showing the intracellular localization of wild-type (WT) or mutated NS1 (Δ20 and Δ30) in cells transfected with NS1-capped mRNA (top panels) or infected by mutant viruses (bottom panels). NS1: rabbit anti-NS1 primary antibody and anti-rabbit Alexa 488-coupled secondary antibody; NS2: component of the viral inclusion bodies, mouse anti-NS2 primary antibody and anti-mouse Alexa 546-coupled secondary; nuclei, blue (Hoechst staining). Experiments were repeated twice independently with similar results. **c**, Transmission electron microscopy analysis of sections of cells infected with wild-type and mutant viruses as indicated. Viral inclusion bodies are indicated (black arrows). Tubules (yellow arrow) are only present in the cytoplasm of cells infected by the wild-type virus. Scale bars, 200 nm. Sectioning data are the result of one experiment. **d**, Growth curves of viruses. Virus titres were determined in triplicates. **e**, Quantification of Renilla luciferase expression by wild-type or mutant NS1. Luciferase activity was detected 24 h after cells were co-transfected with S10-Rluc and wild-type or mutated NS1-capped mRNA. Bars represent the averages of at least three independent experiments (wild type, $n = 7$; mutants, $n = 3$). Distribution of the data and respective P values are indicated (one-tailed t-test: two-sample assuming equal variance, confidence level of 95%). w/o, without.

Δ30 (Δ522–552) were generated using the NS1-encoding gene S5 (Fig. 3a), and their effects on virus replication were assessed using reverse genetics[13]. Both mutant viruses were recovered successfully (Fig. 3b), indicating that virus replication was not significantly hampered. However, we did not observe the characteristic cytoplasmic distinct granular distribution of NS1 (left panels in Fig. 3b) exhibited in wild-type transfected or virus-infected cells, but rather diffuse patterns of NS1 present throughout the cytoplasm (middle

and right panels in Fig. 3b). However, there was no obvious difference in the plaque phenotype between mutant viruses and the wild-type virus (Supplementary Fig. 4), although no tubules were observed by electron microscopy of infected cells (Fig. 3c). Nonetheless, the growth rate of the mutant viruses decreased slightly compared to the wild-type virus (Fig. 3d). Using a reporter RNA assay[4], we tested both Δ20 and Δ30 for their ability to specifically enhance viral protein expression, as described in Methods. In each case, expression of the reporter was detected (Fig. 3e), indicating that NS1 function was not perturbed by the C-terminal deletion. The recovery of these mutant viruses demonstrates that the C-terminal arm and its β-sheet augmentation role are required for tubule formation, but not for the function of NS1 in protein expression, demonstrating that the non-tubular form of NS1 is functional. The characteristic shape of this C-terminal arm linking another monomer suggests that it facilitates dimer formation.

NS1 contains two zinc-finger-like motifs that are important for virus replication and tubule formation. Each NS1 monomer contains two zinc-finger-like motifs: motif 1 and motif 2 (Fig. 4a). Both motifs have a tetrahedral arrangement of side-chain rotamers and a strong density at the centre of the tetrahedron, characteristic of metal coordination in typical zinc-finger motifs. The putative metal ion coordination site of motif 1 is formed by a tetrahedral arrangement of C30, H32, C37 and C43 (Fig. 4a, orange panel). In the tubular form, pairs of foot domains, head domains and C-terminal arms cage motif 1 in tubular NS1, rendering it inaccessible from both outside and inside the tubule. By contrast, motif 1 in both NS1 monomer (Fig. 4a) and NS1 dimer (Fig. 2c) forms are readily accessible. The tetrahedral metal ion coordination site of motif 2 is located at the junction between the head and body domains and is formed by C337, C340, H375 and H398 (Fig. 4a, yellow panel). Its secondary structure arrangement is reminiscent of, but distinct from, typical Cys2His2 zinc fingers, which exhibit a αββ architecture. H375 and H398 reside on separate strands of a three-stranded β-sheet, and are connected by a loop and strand. C337 and C340 are located on h16 at the base of the head domain.

To verify that these motifs are divalent metal ion coordination motifs, we treated tubules with chelating agent and examined the structural changes. The integrity of tubules was compromised by such treatment, leading to fluffy aggregates, which can be restored by divalent cations, including Zn^{2+} (Fig. 4b). This observation indicates that the presence of divalent metal ions may be important for the maintenance of tubular NS1 and that the conversion between the tubular and non-tubular forms is reversible by the removal and addition of metal cations.

To determine the importance of these putative zinc-binding motifs, substitution mutations (C30S, C43S and H32A in motif 1 and C340S, H375A and H398A in motif 2) were generated by site-directed mutagenesis in the viral genome. Each mutation in motif 1 and motif 2 failed to recover viruses by reverse genetics, although a virus was recovered successfully when nearby residues were mutated (KR34-35AA) (Supplementary Fig. 4). Expression of NS1 in each case was visualized by immunofluorescence, although their cytoplasmic distribution was diffused (middle and bottom rows in Fig. 4c). By contrast, the wild-type NS1 and the positive control KR34-35AA NS1 mutant showed the same characteristic cytoplasmic distribution (top row, Fig. 4c). Given that zinc fingers are often involved in nucleic acid binding, it is possible that either of the metal ion coordination motifs is important for structural stability and/or related to the ability of NS1 to selectively upregulate viral mRNA in host cells[4]. However, mutations in motif 1 had no significant effect on the upregulation of the reporter expression, except the H32A mutant, which showed only a slight decrease in the transfected cells (Fig. 4d, orange bars). By contrast, all mutations in motif 2 had drastic effects (up to 21 fold) on the luciferase expression (Fig. 4d, yellow bars), indicating that motif 2 is particularly important to upregulate viral gene translation, although both metal ion coordination motifs are necessary to maintain the characteristic tubular structure.

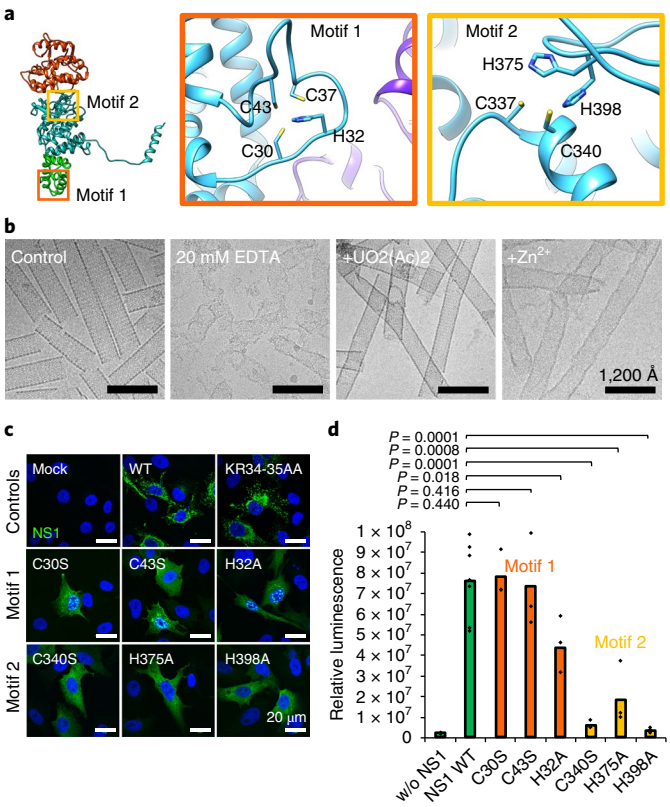

Fig. 4 | NS1 contains two putative zinc-finger motifs, which are important for virus replication and tubule formation. a, Ribbon diagram of an NS1 monomer showing the locations (left) and details (insets) of putative metal ion-binding motifs 1 and 2. The four residues implicated in the tetrahedral coordination in each motif are labelled in the insets. **b**, CryoEM micrographs of well-structured tubules (control), of disrupted tubules in the presence of 20 mM EDTA and of tubules recovered upon addition of divalent uranyl and zinc ions. The experiment was repeated twice independently with similar results. **c**, Immunofluorescence analysis showing the intracellular localization of wild-type or mutated NS1 (motif 1: C30S, C43S and H32A; motif 2: C340S, H375A and H398A) in cells transfected with the respective capped mRNA. The KR34-35AA mutant was used as a control. NS1, rabbit anti-NS1 primary antibody and anti-rabbit Alexa 488-coupled secondary antibody; nuclei, blue (Hoechst staining). Experiments were repeated twice independently with similar results. **d**, Quantification of Renilla luciferase expression by wild-type NS1 or NS1 harbouring putative zinc-finger motif mutations. Luciferase activity was detected 24 h after cells were co-transfected with S10-Rluc and wild-type or mutated NS1-capped mRNA. Bars represent the averages of at least three independent experiments (wild type, $n=7$; mutants, $n=3$). Distribution of the data and respective P values are indicated (one-tailed t-test: two-sample assuming equal variance, confidence level of 95%).

Intra-layer monomer–monomer interactions. Two large binding surfaces spanning the length of the NS1 protein are presented by each monomer to its two neighbouring monomers within the same layer. These interfaces (A and B) include a mixture of hydrophobic and charged residues (Figs. 1c and 5a), dictating extensive interactions between monomers of the same layer. Interface B revealed many interactions, including a possible disulfide bond formation between C364 of one monomer and C364 of the other monomer

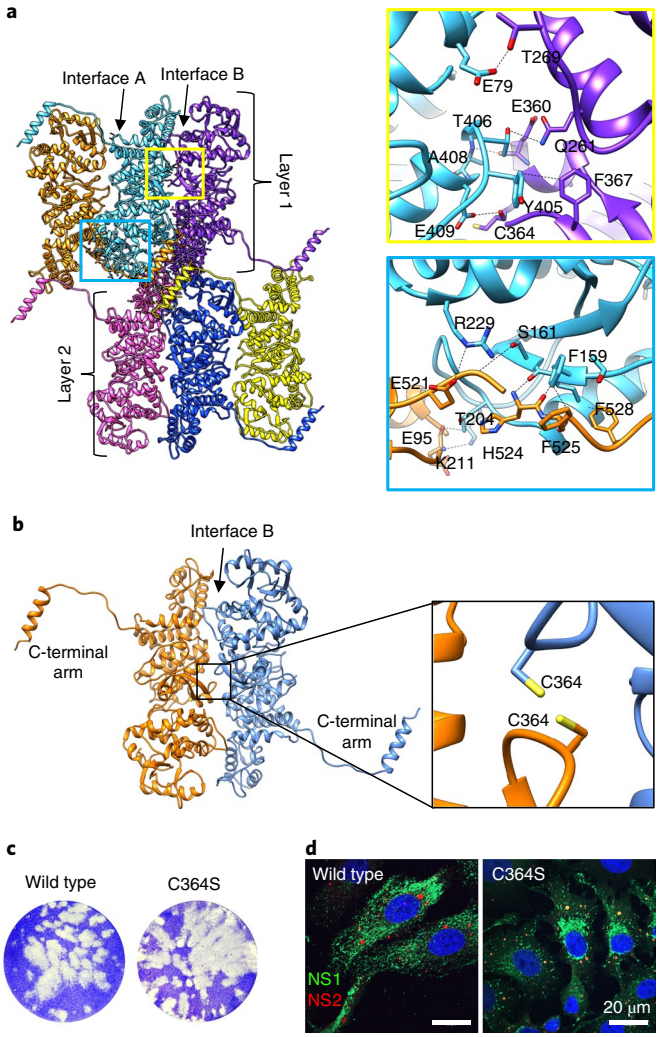

Fig. 5 | Inter-layer and intra-layer interactions in NS1 tubules. a, Inter-layer six-monomer junction in the NS1 tubule. Blue inset, atomic models showing intra-layer β-sheet augmentation involving the head domain of one monomer and the C-terminal arm of the other monomer. Yellow inset, atomic models of sample intra-layer packing between the head domain of one monomer and the foot domain of another monomer. Monomer–monomer interfaces A and B are indicated. **b**, Putative disulfide bond between monomers of the same layer. Black inset, atomic models of the C364 side-chain position and orientation. **c**, Recovery of the C364S mutant virus by reverse genetics compared to the wild-type virus. Plaques (white) indicative of recovered viruses were visualized by crystal violet staining. Similar plaque phenotypes were observed for the wild-type and mutant viruses. **d**, Intracellular localization of wild-type or C364S mutant NS1. Immunofluorescence analysis showed similar viral inclusion bodies (indicative of similar viral recovery) but partially affected intracellular NS1 localization in cells infected with the mutant virus compared to those infected with the wild-type virus. NS1: rabbit anti-NS1 primary antibody and anti-rabbit Alexa 488-coupled secondary antibody, NS2: component of the viral inclusion bodies; mouse anti-NS2 primary antibody and anti-mouse Alexa 546-coupled secondary antibody; nuclei, blue (Hoechst staining). Experiments were repeated twice independently with similar results (**c**,**d**).

in the same layer around a sideway two-fold symmetry axis (Fig. 5b). Previous studies using recombinant NS1 protein showed that a C364S mutant formed tubules similar to wild-type NS1 (ref. [14]). To investigate in the context of virus infection, we created the same mutation in the viral genome and successfully recovered the C364S mutant virus with a similar plaque phenotype to the wild-type virus (Fig. 5c). Cells infected with plaque-purified wild-type or C364S mutant viruses showed efficient viral replication, although the intracellular localization of NS1 C364S was slightly affected (Fig. 5d). Taken together, these results indicate that such a disulfide bond is unlikely to be critical to tubule formation and suggest that interface B is complex and will need further studies.

Discussion

In this study, we obtained an atomic model of BTV NS1, derived from a near-atomic resolution cryoEM helical reconstruction of NS1 tubules. The observation of multiple, dynamic classes of tubules indicate that NS1 monomers are able to assemble with some degree of flexibility, without affecting the monomeric structure. This ability to form tubules of variable helical forms and diameter suggests that tubule formation is a robust process capable of initiating in various configurations. The helical reconstruction shows that the immunogenic C terminus is located along the tubule surface, consistent with several previous studies, which indicated to this localization[12,15]. The location of the C terminus rationalizes the ability of NS1 tubules to serve as effective immunogen delivery vehicles, capable of carrying large peptides without disrupting the tubular structure[15–17]. The structure-based mutagenesis studies showed that deleting the NS1 C-terminal arm abrogated tubule formation, but still could recover infectious virus and retained the ability to regulate viral protein expression as confirmed by a reporter assay. Thus, the non-tubular form of NS1 is sufficient for virus replication and for upregulating viral mRNA translation. Although the tubular form is not required for upregulating viral RNA translation, tubule formation during BTV infection had been reported to reduce cytopathic effects, suggesting that NS1 tubules may play a role in cellular pathogenesis[18,19].

Our NS1 structure shares no recognizable similarity with any published structures. During rotavirus infection, the non-structural viral protein NSP3A acts like cellular poly(A)-binding protein 1 and binds to the 3′ end of viral mRNA[2]. Motifs implicated in dimerization, RNA binding and interaction with eukaryotic translation initiation factor 4G1 (eIF4G1) have been mapped in rotavirus NSP3 (ref. [3]), and although both N-terminal and C-terminal domain structures of NSP3 were described, neither significant sequence identity nor structural similarity between BTV NS1 and rotavirus NSP3 can be recognized[7,8]. A human cellular protein conserved in mammals, termed rotavirus 'X'-associated non-structural protein (RoXaN), has been shown to form a ternary complex with eIF4G and rotavirus NSP3 (ref. [5]), thereby promoting interaction between cytoplasmic poly(A)-binding protein and viral RNA[6]. Surprisingly, RoXaN bears some sequence similarity to BTV NS1 at the solvent-exposed regions except for the C-terminal arm, with 94 identical and 177 similar amino acid residues (Supplementary Fig. 2). Given that NS1 is known to selectively upregulate viral protein synthesis by binding to the 3′ end of viral mRNA[4], we speculate that NS1 may mimic some function of RoXaN, plausibly promoting interaction between viral mRNA and eIF4G or other components of the host translation machinery to upregulate viral protein synthesis.

Our atomic structure of BTV NS1 reveals two zinc-finger-like motifs with tetrahedral arrangements, motif 1 and motif 2, and our functional studies revealed that the tubule structure was significantly affected by chelating agent treatment. Remarkably, RoXaN possesses five similar motifs (C3H1 and C2H2 types). The first of these five motifs is localized to a region with 100% identity with BTV NS1's motif 2 (337-CQLCY-341; Supplementary Fig. 2b), which is necessary for NS1 to fulfil its upregulation function of viral mRNA translation. By contrast, the region around motif 1 of BTV NS1 aligns with RoXaN only in a limited manner (Supplementary Fig. 2b). Zinc-finger motifs are known to stabilize protein structure, or to bind to nucleic acids, or to mediate protein–protein interactions[20,21]. Our data show that, although motif 2 plays a major role for

the upregulation of viral protein translation, the integrity of both motifs is probably essential for maintaining the stability of the NS1 structure. In addition, typical granulated patterns observed in the cells transfected with wild-type NS1 were not present in the mutant NS1-transfected cells, consistent with our conclusion that these motifs are likely to be important for the tubule stability. However, how NS1 zinc-finger motifs upregulate BTV replication awaits further investigation. Nevertheless, we do not rule out possibilities that these motifs bind alternatively to some other, unidentified metal ions[22]. Selection pressure has forced organisms to evolve complex regulation processes for gene expression regulation, through multiple levels of control and involving many molecules of nucleic acids and proteins. Facing the scarcity of resources, a simple organism such as a virus has to employ different strategies to regulate its gene expression, including using multiple oligomeric states of a single protein. Considering the fact that the tubules, purified from BTV-infected cells, assemble in variable helical forms that can be converted to non-helical forms by the level of zinc or other divalent cations, we hypothesize that BTV might employ a negative-feedback mechanism to regulate viral protein translation by sequestering the functional non-tubular form of NS1 into tubular assemblies. This process may involve regulation of the local concentration of metal ions. As BTV is a model virus system for many double-stranded RNA viruses, these findings offer a rare glimpse into the regulatory aspect of the viral life cycle[23], while simultaneously providing a trove of information on both tubular and non-tubular forms of NS1 and the relationship between the two forms. It opens the door to new possibilities in structure–function relationship studies to allow further understanding of NS1–host cell machinery interaction.

Methods

Cells and viruses. BSR cells (BHK-21 subclone) were cultured in DMEM supplemented with 5% (v/v) FBS at 35 °C in 5% CO_2.

Wild-type and mutant BTV viruses were recovered by reverse genetics as previously described[13] (see below). Each recovered virus was plaque purified, amplified in BSR cells and harvested at 100% cytopathic effect between 2 and 3 days. Viruses were titrated either using a plaque assay or a TCID50 (50% tissue culture infectious dose) assay.

Tubule purification. BSR cells were infected with wild-type or mutant BTV1 at multiplicity of infection of 0.5 during 1 h. Viral inoculum was subsequently removed and cells were incubated in 1% FBS culture medium for 44 h until 100% cytopathic effect. Supernatant and cells were harvested and clarified for 10 min at 4,500 r.p.m. Cell pellets were resuspended in pre-chilled lysis buffer (100 mM Tris HCl, pH 7.5, 50 mM NaCl, 10 mM EDTA and 0.1% NP-40 (Sigma)), incubated at 4 °C for 10 min and spun down at 4,000 r.p.m. 5 min at 4 °C. Supernatants were kept on ice and lysis was repeated once. Supernatants were pooled and loaded on a 40% w/v sucrose cushion in 20 mM Tris HCl, pH 7.5, and 150 mM NaCl buffer. Ultracentrifugation was carried out at 28,000 r.p.m. at 4 °C for 2 h. The pellet was resuspended overnight in 20 mM Tris HCl, pH 7.5, and 150 mM NaCl buffer prior to vitrification for cryoEM sample preparation.

CryoEM. Optimization for sample distribution and ice thickness was performed in an FEI TF20 cryoEM equipped with a TVIPS 16 MP CCD camera, first by negative stain and then by cryoEM. High-resolution cryoEM images were recorded in a Titan Krios instrument over a 10-year period in an effort to improve the resolution of the structure. Two different types of cryoEM micrographs were recorded and processed in this effort. Prior to the advent of direct electron detectors, we recorded cryoEM images on photographic films (film data set). However, after exhaustive efforts and 2,087 films, we were unable to improve our 3D structure to be better than a 4.5-Å resolution. For this reason, when electron counting became available to us, we imaged the same tubules again in a Gatan K2 Summit direct electron camera attached to an energy filter. The direct electron detector data set of cryoEM images was collected as movies in an FEI Titan Krios microscope (operated at 300 kV) equipped with a Gatan imaging filter (the slit was not inserted) and a K2 Summit direct electron camera in counting mode using the Leginon software package[24] for automation. The target defocus value was set to 2.0 µm under focus. Each movie contains 50 frames with 5 frames per second, with a total accumulated dosage of 60 electrons per Å^2. The dose rate is measured at 6 electrons per Å^2 per second in the Digital Micrograph software package, which is calibrated to 7.5 electrons per Å^2 per second compared to our initial efforts with films[25,26]. A total of 5,006 movies were collected over two sessions.

Image processing for the film data. Micrographs recorded on Kodak SO163 photographic films were digitized and screened to select tubules that are non-overlapping, intact and free of ice contamination. Tubule particles were manually selected with EMAN[27] helixboxer with a box width of 640 and was segmented according to a 10% overlapping scheme. A total of 218,238 segments were selected from images from all sessions. The contrast transfer function parameters of these movies were determined by CTFFIND3 (ref. [28]). The determined defocus range was 0.6–3.1 µm.

We carried out reference-free 2D classifications (tier I) of these particles by EMAN refine2d.py. The resulting class averages show different tube diameters. We further classified these classes manually by their diameters (four different diameters). For each meta-class (tier II), all class-average images were transformed into Fourier space so that their amplitude images (layer line images) were translated into real-space images. These images were classified again in 2D (tier III, 10 classes). For every tier II class, we noticed that there are three modes (tier IV) of peri-meridian reflections in the 10 (tier III) class averages. These four tiered classification suggested that there are 12 (4×3) different helical forms in the population of particles.

We indexed every tier IV class average as previously described by David DeRosier (http://www.biomachina.org/courses/structures/download/derosier_handout_02.pdf) and ref. [29]. Basically, the three modes of peri-meridian reflections put (0,1) at $n=1$, 2 and 3, respectively (one-, two- and three-start helices). Surprisingly, for all helices, the pitches are roughly the same, being ~88–89 Å; however, their l numbers are different. The selection rule for all three helical form of class 2 diameter helices (tier II), as determined from (0,1) and (1,0) reflections are ($l=-5n+101$ m; $n=20$, $l=1$ and $n=-1$, $l=5$), ($l=-7n+144$ m; $n=20$, $l=4$ and $n=2$, $l=14$) and ($l=-11n+232$ m; $n=20$, $l=12$ and $n=-3$, $l=33$) (Supplementary Fig. 3). Other helical forms can be deduced in a similar way.

We sorted the particles according to their tier IV class identities and calculated a volume for each of them by EMAN-based IHRSR[25,30]. Further image processing steps were performed with Relion v1.2 with IHRSR[31]. The selected particles for tier II class 2–tier IV class 1 (20.2 dimers per turn, tier IV grand rank #4), tier II class 2–tier IV class 2 (20.57 dimers per turn, tier IV grand rank #5), tier II class 3–tier IV class 1 (21.2 dimers per turn, tier IV grand rank #7) and tier II class 2–tier IV class 2 (21.57 dimers per turn, tier IV grand rank #8) were refined with Relion v1.2, respectively. The final resolutions for resulting maps are in the 4.5–5.0-Å range, marginally unsuitable for atomic modelling.

Image processing for the direct electron detector data. Frames within each movie were aligned to correct for drift as previously described[32], except that an iterative alignment scheme was used as previously described elsewhere[33]. Aligned frames were averaged to generate two average micrographs for different purposes: one by averaging the 1st to 50th frames for particle selection and determination of contrast transfer function parameters, and the other by averaging 3rd to 20th frames for structure refinement. Contrast transfer function parameters were determined by CTFFIND3 (ref. [28]), and those with very large and very small underfocus values were discarded. The determined defocus ranges for included data were 1.2–4 µm for session 1 and 1.5–3.5 µm for session 2.

Tubule particles were manually selected the same way as with the film data set except for a 720 box width and was segmented according to a 10% overlapping scheme; a total of 87,190 segments were selected for images from both sessions. We cleaned up the particles using Relion v1.4 Class2D.

For each session, all particles were subjected to a Class3D run with 12 classes for the separation of the 12 helical forms. For each helical form, particles from the two sessions were combined. We further analysed the helical forms of 20.2 dimers per turn (grand rank #4) and 20.57 dimers per turn (grand rank #5), respectively.

For each of the two selected helical forms, a Class3D run with five classes was done to separate particles at different stages of thermal breathing of the tube. Only the class with the most particles—incidentally, the class with the medium diameter—was included for further processing, respectively.

We initially used Refine3D in Relion v2.0 to refine the structures. However, given the signal-to-noise-ratio-based regularization intrinsic to the Relion algorithm, a working resolution control was not satisfactory, as there are too many helically related copies, and signal-to-noise ratio compensation that worked for previous studies with less helically related copies[31] did not work properly. Thus, we used Class3D with one class to refine the structures and manually adjusted T factor (--tau_fudge) and healpix order so that the refinement could progress.

We then first averaged the two monomers in the dimers from the 1-start helical form with Chimera[34]. The monomers were automatically averaged in the 2-start helical form as dihedral (D2) symmetry was imposed during refinement. We then averaged the dimers across two helical forms with Chimera[34].

Atomic model building. The backbone of the NS1 monomer was traced using Coot[35]. The PHYRE2 (ref. [36]) prediction server was used to partially guide backbone tracing. The backbone coordinates were then changed to peptide and subsequently mutated to the correct sequence. The initial N terminus assignment was corrected to account for a twofold symmetry axis. The subsequent model went through manual regularization using Coot[37], before undergoing real-space refinement through PHENIX[38]. The output was analysed using the Molprobity[39]

integration in Coot and had its clashscore and geometry improved manually. The structure was then subjected to geometry_minimization in PHENIX and then fed to real-space refinement with simulated annealing, using MolProbity functions built into PHENIX to track model quality and agreement with the density map throughout refinement. The final model was checked for fitting errors manually in Coot and UCSF Chimera[34]. All structural figures were generated using UCSF Chimera.

Plasmids. The plasmids used in this study were pCAGGS BTV1 protein expression plasmids (pCAG-VP1, pCAG-VP3, pCAG-VP4, pCAG-VP6 and pCAG-NS2) and T7 plasmids for BTV transcripts as previously described[13].

Site-directed mutagenesis. Site-directed mutagenesis of BTV1 NS1 was performed using the T7 segment 5 (encoding NS1) template and the following mutagenic primers (5′–3′):

C30S (CCACAATGGACTAGCAGTCATCTAAAAAGG),
C43S (GGAATTGTTTATTCAATGGGATGAGTGTTAAACAAAATTTTGA GAGAGC),
H32A (CAATGGACTTGCAGTGCTCTAAAAAGGAATTG),
KR34-35AA (GGACTTGCAGTCATCTAGCAGCGAATTGTTTATTCAATGG),
C340S (GCATACATGTCAGCTGAGCTACTTGAAACACTC),
C364S (CATCAGAACTAACTGGGTCTTCGCCATTCAAGACGG),
H375A (GTGAAGATTGAGGAAGCTGTGGGAAATGATTCG),
H398A (GGCAGGATCGGAGATGCTTATTATACTACAAATTG),
Δ20 (GCTGGGTTCGCGGCACCTGCGTAGTTACTGACTTCTGTT),
Δ30 (CCCTATGCTATGCAGAAAAGTAGTTACTGACTTCTGTTTTCTG).

Mutagenic bases are underlined. Obtained mutants were subsequently sequenced using an internal NS1 primer to confirm the presence of the desired mutation(s).

Synthesis of NS1-capped mRNAs. Synthetic single-stranded RNAs were prepared by run-off in vitro transcription from T7 PCR products using T7 RNA polymerase. Transcripts were prepared with anti-reverse cap analogue using the mMESSAGE mMACHINE T7 Ultra Kit (Ambion) as previously described[13]. Transcripts were analysed by electrophoresis in 1% agarose in morpholinepropanesulfonic acid in the presence of formaldehyde.

Transfection of BSR cells. Seventy per cent confluent BSR monolayers in 12-well plates were transfected with 500 ng mRNA transcripts using Endofectin (GeneCopoeia), according to the manufacturer's instructions. Cells were subsequently incubated at 35 °C in 5% CO_2 8–24 h after transfection.

Reporter RNA transcript preparation and quantification of reporter expression. Reporter RNAs were prepared and the quantification of reporter expression was performed as previously described[4] with slight modifications. Briefly, the pS10-Rluc plasmid clone containing the 5′ 152 nucleotides and 3′ 149 nucleotides of BTV-1 segment 10 fused with the Renilla luciferase gene was digested with restriction enzymes, and synthetic capped single-stranded RNAs were prepared by run-off in vitro transcription using the mMESSAGE mMACHINE T7 Ultra Kit (Ambion). BSR 96-well monolayers were transfected with 150 ng capped S5 RNA wild-type or mutant and 150 ng capped S10-Rluc reporter RNA. Renilla luciferase expression in the transfected cell lysates was quantified in triplicates 24 h after transfection with a Turner Biosystems Glomax luminometer with Promega's dual luciferase reporter assay system according to the manufacturer's instructions.

Recovery of viruses by reverse genetics. Reverse genetics was performed as previously described[13]. Briefly, at day 1, 70–80% confluent BSR monolayers were transfected with pCAG-VP1, pCAG-VP3, pCAG-VP4, pCAG-VP6 and pCAG-NS2 (120 ng each) using Endofectin (GeneCopoeia), according to the manufacturer's instructions, and incubated at 35 °C in 5% CO_2 overnight. At day 2, the cells were transfected with each BTV1 exact copies RNA transcripts (S5 wild type or mutated) using Endofectin (GeneCopoeia), overlaid with 1% agarose and incubated for 3 days at 35 °C in 5% CO_2. Visible plaques were picked up and resuspended in 1% FBS containing medium, and/or cells were subsequently fixed with 10% formaldehyde and stained with crystal violet.

Immunofluorescence assays. BSR cells were grown on coverslips and either transfected with capped mRNA or infected with wild-type or mutant viruses. Eight to ten hours post-transfection or infection, cells were fixed with 4% paraformaldehyde (Sigma) solution, permeabilized with 0.5% Triton X-100 (Sigma), blocked with 1% BSA (Sigma) and subsequently stained using rabbit anti-NS1 and/or mouse anti-NS2 primary antibodies, and anti-rabbit Alexa 488 or anti-mouse Alexa 546 coupled secondary antibodies (Thermo Fisher Scientific). Nuclei were stained using Hoechst 33342 (Thermo Fisher Scientific). Images were acquired using an ×100 oil objective and a Zeiss Axiovert LSM510 confocal microscope supplied with the LSM510 software.

Cell sectioning analysis. BSR cells were infected at multiplicity of infection of 5 and were processed for cell sectioning at 16 h post-infection. Briefly, monolayers were fixed in 2% paraformaldehyde, 1.5% glutaraldehyde and 0.1 M sodium cacodylate buffer (pH 7.3) and post-fixed in 1% osmium tetroxide, 1.5% potassium ferrocyanide and 0.2 M sodium cacodylate buffer. Cells were dehydrated in increasing concentrations of ethanol and embedded in epoxy resin (TAAB Laboratories Equipment). Ultrathin sections were stained with lead citrate.

Reporting Summary. Further information on research design is available in the Nature Research Reporting Summary linked to this article.

Data availability

The atomic models and cryoEM density map that support the findings of this study have been deposited in the Protein Data Bank and Electron Microscopy Data Bank with accession numbers 6N9Y and EMD-0383, respectively.

Received: 16 October 2018; Accepted: 11 January 2019;
Published online: 18 February 2019

References

1. Walsh, D. & Mohr, I. Viral subversion of the host protein synthesis machinery. *Nat. Rev. Microbiol.* **9**, 860–875 (2011).
2. Piron, M., Vende, P., Cohen, J. & Poncet, D. Rotavirus RNA-binding protein NSP3 interacts with eIF4GI and evicts the poly(A) binding protein from eIF4F. *EMBO J.* **17**, 5811–5821 (1998).
3. Piron, M., Delaunay, T., Grosclaude, J. & Poncet, D. Identification of the RNA-binding, dimerization, and eIF4GI-binding domains of rotavirus nonstructural protein NSP3. *J. Virol.* **73**, 5411–5421 (1999).
4. Boyce, M., Celma, C. P. & Roy, P. Bluetongue virus non-structural protein 1 is a positive regulator of viral protein synthesis. *Virol. J.* **9**, 178 (2012).
5. Vitour, D., Lindenbaum, P., Vende, P., Becker, M. M. & Poncet, D. RoXaN, a novel cellular protein containing TPR, LD, and zinc finger motifs, forms a ternary complex with eukaryotic initiation factor 4G and rotavirus NSP3. *J. Virol.* **78**, 3851–3862 (2004).
6. Harb, M. et al. Nuclear localization of cytoplasmic poly(A)-binding protein upon rotavirus infection involves the interaction of NSP3 with eIF4G and RoXaN. *J. Virol.* **82**, 11283–11293 (2008).
7. Deo, R. C., Groft, C. M., Rajashankar, K. R. & Burley, S. K. Recognition of the rotavirus mRNA 3′ consensus by an asymmetric NSP3 homodimer. *Cell* **108**, 71–81 (2002).
8. Groft, C. M. & Burley, S. K. Recognition of eIF4G by rotavirus NSP3 reveals a basis for mRNA circularization. *Mol. Cell* **9**, 1273–1283 (2002).
9. Hewat, E. A., Booth, T. F., Wade, R. H. & Roy, P. 3-D reconstruction of bluetongue virus tubules using cryoelectron microscopy. *J. Struct. Biol.* **108**, 35–48 (1992).
10. Urakawa, T. & Roy, P. Bluetongue virus tubules made in insect cells by recombinant baculoviruses: expression of the NS1 gene of bluetongue virus serotype 10. *J. Virol.* **62**, 3919–3927 (1988).
11. Odom, T. W., Huang, J. L. & Lieber, C. M. Single-walled carbon nanotubes: from fundamental studies to new device concepts. *Ann. N. Y. Acad. Sci.* **960**, 203–215 (2002).
12. Monastyrskaya, K., Gould, E. A. & Roy, P. Characterization and modification of the carboxy-terminal sequences of bluetongue virus type 10 NS1 protein in relation to tubule formation and location of an antigenic epitope in the vicinity of the carboxy terminus of the protein. *J. Virol.* **69**, 2831–2841 (1995).
13. Boyce, M., Celma, C. C. & Roy, P. Development of reverse genetics systems for bluetongue virus: recovery of infectious virus from synthetic RNA transcripts. *J. Virol.* **82**, 8339–8348 (2008).
14. Monastyrskaya, K., Booth, T., Nel, L. & Roy, P. Mutation of either of 2 cysteine residues or deletion of the amino or carboxy-terminus of nonstructural protein Ns1 of bluetongue virus abrogates virus-specified tubule formation in insect cells. *J. Virol.* **68**, 2169–2178 (1994).
15. Mikhailov, M., Monastyrskaya, K., Bakker, T. & Roy, P. A new form of particulate single and multiple immunogen delivery system based on recombinant bluetongue virus-derived tubules. *Virology* **217**, 323–331 (1996).
16. Ghosh, M. K., Borca, M. V. & Roy, P. Virus-derived tubular structure displaying foreign sequences on the surface elicit $CD4^+$ Th cell and protective humoral responses. *Virology* **302**, 383–392 (2002).
17. Murphy, A. & Roy, P. Manipulation of the bluetongue virus tubules for immunogen delivery. *Future Microbiol.* **3**, 351–359 (2008).
18. Owens, R. J., Limn, C. & Roy, P. Role of an arbovirus nonstructural protein in cellular pathogenesis and virus release. *J. Virol.* **78**, 6649–6656 (2004).
19. Mortola, E., Noad, R. & Roy, P. Bluetongue virus outer capsid proteins are sufficient to trigger apoptosis in mammalian cells. *J. Virol.* **78**, 2875–2883 (2004).
20. Hall, T. M. Multiple modes of RNA recognition by zinc finger proteins. *Curr. Opin. Struct. Biol.* **15**, 367–373 (2005).

21. Laity, J. H., Lee, B. M. & Wright, P. E. Zinc finger proteins: new insights into structural and functional diversity. *Curr. Opin. Struct. Biol.* **11**, 39–46 (2001).
22. Attar, N. et al. The histone H3–H4 tetramer is a copper reductase enzyme. Preprint at https://www.biorxiv.org/content/early/2018/06/19/350652 (2018).
23. Yu, X., Jiang, J., Sun, J. & Zhou, Z. H. A putative ATPase mediates RNA transcription and capping in a dsRNA virus. *eLife* **4**, e07901 (2015).
24. Carragher, B. et al. Leginon: an automated system for acquisition of images from vitreous ice specimens. *J. Struct. Biol.* **132**, 33–45 (2000).
25. Ge, P. & Zhou, Z. H. Hydrogen-bonding networks and RNA bases revealed by cryo electron microscopy suggest a triggering mechanism for calcium switches. *Proc. Natl Acad. Sci. USA* **108**, 9637–9642 (2011).
26. Zhang, X., Jin, L., Fang, Q., Hui, W. H. & Zhou, Z. H. 3.3 Å cryo-EM structure of a nonenveloped virus reveals a priming mechanism for cell entry. *Cell* **141**, 472–482 (2010).
27. Ludtke, S. J., Baldwin, P. R. & Chiu, W. EMAN: semi-automated software for high resolution single particle reconstructions. *J. Struct. Biol.* **128**, 82–97 (1999).
28. Mindell, J. A. & Grigorieff, N. Accurate determination of local defocus and specimen tilt in electron microscopy. *J. Struct. Biol.* **142**, 334–347 (2003).
29. Diaz, R., Rice, W. J. & Stokes, D. L. Fourier–Bessel reconstruction of helical assemblies. *Methods Enzymol.* **482**, 131–165 (2010).
30. Egelman, E. H. The iterative helical real space reconstruction method: surmounting the problems posed by real polymers. *J. Struct. Biol.* **157**, 83–94 (2007).
31. Ge, P. et al. Atomic structures of a bactericidal contractile nanotube in its pre- and postcontraction states. *Nat. Struct. Mol. Biol.* **22**, 377–382 (2015).
32. Clemens, D. L., Ge, P., Lee, B. Y., Horwitz, M. A. & Zhou, Z. H. Atomic structure of T6SS reveals interlaced array essential to function. *Cell* **160**, 940–951 (2015).
33. Bartesaghi, A. et al. 2.2 Å resolution cryo-EM structure of beta-galactosidase in complex with a cell-permeant inhibitor. *Science* **348**, 1147–1151 (2015).
34. Pettersen, E. F. et al. UCSF Chimera—a visualization system for exploratory research and analysis. *J. Comput. Chem.* **25**, 1605–1612 (2004).
35. Emsley, P. & Cowtan, K. Coot: model-building tools for molecular graphics. *Acta Crystallogr. D Biol. Crystallogr.* **60**, 2126–2132 (2004).
36. Kelley, L. A., Mezulis, S., Yates, C. M., Wass, M. N. & Sternberg, M. J. The Phyre2 web portal for protein modeling, prediction and analysis. *Nat. Protoc.* **10**, 845–858 (2015).
37. Emsley, P., Lohkamp, B., Scott, W. G. & Cowtan, K. Features and development of Coot. *Acta Crystallogr. D Biol. Crystallogr.* **66**, 486–501 (2010).
38. Adams, P. D. et al. PHENIX: a comprehensive Python-based system for macromolecular structure solution. *Acta Crystallogr. D Biol. Crystallogr.* **66**, 213–221 (2010).
39. Chen, V. B. et al. MolProbity: all-atom structure validation for macromolecular crystallography. *Acta Crystallogr. D Biol. Crystallogr.* **66**, 12–21 (2010).

Acknowledgements

We thank M. Turmaine for his advice and support for imaging at the UCL EM facility and C. Celma (LSHTM) for advising in the BTV reverse genetics method. This project is supported partly by grants from the US NIH (AI094386 to Z.H.Z.) and The Wellcome Trust, UK (100218, Investigator Award to P.R.). We acknowledge the use of instruments at the Electron Imaging Center for Nanomachines supported by UCLA and grants from the NIH (1S10OD018111 and 1U24GM116792) and the National Science Foundation (DBI-1338135 and DMR-1548924). This work used the Extreme Science and Engineering Discovery Environment (XSEDE), which is supported by the National Science Foundation grant number ACI-1548562 (Comet cluster at the San Diego Supercomputing Center through allocation MCB140140).

Author contributions

Z.H.Z., P.R. and P.G. designed the experiments. M.B. purified the wild-type NS1 tubules. X.Z. recorded some of the cryoEM data. P.G. recorded the cryoEM data and determined the structure. M.L. and J.J. built the atomic models. A.K. expressed proteins, performed the mutagenesis and biochemical experiments, reverse genetics, virology and fluorescence microscopy analyses. M.L., Z.H.Z., P.R., P.G. and A.K. interpreted the data and wrote the paper.

Competing interests

The authors declare no competing interests.

Additional information

Supplementary information is available for this paper at https://doi.org/10.1038/s41564-019-0369-x.

Reprints and permissions information is available at www.nature.com/reprints.

Correspondence and requests for materials should be addressed to Z.H.Z. or P.R.

Publisher's note: Springer Nature remains neutral with regard to jurisdictional claims in published maps and institutional affiliations.

nature research

Corresponding author(s): Polly Roy - NMICROBIOL-18102157A

Reporting Summary

Nature Research wishes to improve the reproducibility of the work that we publish. This form provides structure for consistency and transparency in reporting. For further information on Nature Research policies, see Authors & Referees and the Editorial Policy Checklist.

Statistical parameters

When statistical analyses are reported, confirm that the following items are present in the relevant location (e.g. figure legend, table legend, main text, or Methods section).

n/a	Confirmed	
☐	☒	The exact sample size (*n*) for each experimental group/condition, given as a discrete number and unit of measurement
☐	☒	An indication of whether measurements were taken from distinct samples or whether the same sample was measured repeatedly
☐	☒	The statistical test(s) used AND whether they are one- or two-sided *Only common tests should be described solely by name; describe more complex techniques in the Methods section.*
☐	☐	A description of all covariates tested
☐	☐	A description of any assumptions or corrections, such as tests of normality and adjustment for multiple comparisons
☐	☐	A full description of the statistics including central tendency (e.g. means) or other basic estimates (e.g. regression coefficient) AND variation (e.g. standard deviation) or associated estimates of uncertainty (e.g. confidence intervals)
☐	☐	For null hypothesis testing, the test statistic (e.g. *F*, *t*, *r*) with confidence intervals, effect sizes, degrees of freedom and *P* value noted *Give P values as exact values whenever suitable.*
☐	☐	For Bayesian analysis, information on the choice of priors and Markov chain Monte Carlo settings
☐	☐	For hierarchical and complex designs, identification of the appropriate level for tests and full reporting of outcomes
☐	☐	Estimates of effect sizes (e.g. Cohen's *d*, Pearson's *r*), indicating how they were calculated
☐	☐	Clearly defined error bars *State explicitly what error bars represent (e.g. SD, SE, CI)*

Our web collection on statistics for biologists may be useful.

Software and code

Policy information about availability of computer code

Data collection	*Provide a description of all commercial, open source and custom code used to collect the data in this study, specifying the version used OR state that no software was used.*
Data analysis	*Provide a description of all commercial, open source and custom code used to analyse the data in this study, specifying the version used OR state that no software was used.*

For manuscripts utilizing custom algorithms or software that are central to the research but not yet described in published literature, software must be made available to editors/reviewers upon request. We strongly encourage code deposition in a community repository (e.g. GitHub). See the Nature Research guidelines for submitting code & software for further information.

Data

Policy information about availability of data

All manuscripts must include a data availability statement. This statement should provide the following information, where applicable:

- Accession codes, unique identifiers, or web links for publicly available datasets
- A list of figures that have associated raw data
- A description of any restrictions on data availability

The atomic models and cryoEM density map that support the findings of this study have been deposited in PDB and EMDB with accession numbers 6N9Y and EMD-0383, respectively.

Field-specific reporting

Please select the best fit for your research. If you are not sure, read the appropriate sections before making your selection.

☐ Life sciences ☐ Behavioural & social sciences ☐ Ecological, evolutionary & environmental sciences

For a reference copy of the document with all sections, see nature.com/authors/policies/ReportingSummary-flat.pdf

Life sciences study design

All studies must disclose on these points even when the disclosure is negative.

Sample size	*Describe how sample size was determined, detailing any statistical methods used to predetermine sample size OR if no sample-size calculation was performed, describe how sample sizes were chosen and provide a rationale for why these sample sizes are sufficient.*
Data exclusions	*Describe any data exclusions. If no data were excluded from the analyses, state so OR if data were excluded, describe the exclusions and the rationale behind them, indicating whether exclusion criteria were pre-established.*
Replication	*Describe the measures taken to verify the reproducibility of the experimental findings. If all attempts at replication were successful, confirm this OR if there are any findings that were not replicated or cannot be reproduced, note this and describe why.*
Randomization	*Describe how samples/organisms/participants were allocated into experimental groups. If allocation was not random, describe how covariates were controlled OR if this is not relevant to your study, explain why.*
Blinding	*Describe whether the investigators were blinded to group allocation during data collection and/or analysis. If blinding was not possible, describe why OR explain why blinding was not relevant to your study.*

Behavioural & social sciences study design

All studies must disclose on these points even when the disclosure is negative.

Study description	*Briefly describe the study type including whether data are quantitative, qualitative, or mixed-methods (e.g. qualitative cross-sectional, quantitative experimental, mixed-methods case study).*
Research sample	*State the research sample (e.g. Harvard university undergraduates, villagers in rural India) and provide relevant demographic information (e.g. age, sex) and indicate whether the sample is representative. Provide a rationale for the study sample chosen. For studies involving existing datasets, please describe the dataset and source.*
Sampling strategy	*Describe the sampling procedure (e.g. random, snowball, stratified, convenience). Describe the statistical methods that were used to predetermine sample size OR if no sample-size calculation was performed, describe how sample sizes were chosen and provide a rationale for why these sample sizes are sufficient. For qualitative data, please indicate whether data saturation was considered, and what criteria were used to decide that no further sampling was needed.*
Data collection	*Provide details about the data collection procedure, including the instruments or devices used to record the data (e.g. pen and paper, computer, eye tracker, video or audio equipment) whether anyone was present besides the participant(s) and the researcher, and whether the researcher was blind to experimental condition and/or the study hypothesis during data collection.*
Timing	*Indicate the start and stop dates of data collection. If there is a gap between collection periods, state the dates for each sample cohort.*
Data exclusions	*If no data were excluded from the analyses, state so OR if data were excluded, provide the exact number of exclusions and the rationale behind them, indicating whether exclusion criteria were pre-established.*
Non-participation	*State how many participants dropped out/declined participation and the reason(s) given OR provide response rate OR state that no participants dropped out/declined participation.*

Randomization | *If participants were not allocated into experimental groups, state so OR describe how participants were allocated to groups, and if allocation was not random, describe how covariates were controlled.*

Ecological, evolutionary & environmental sciences study design

All studies must disclose on these points even when the disclosure is negative.

Study description	*Briefly describe the study. For quantitative data include treatment factors and interactions, design structure (e.g. factorial, nested, hierarchical), nature and number of experimental units and replicates.*
Research sample	*Describe the research sample (e.g. a group of tagged Passer domesticus, all Stenocereus thurberi within Organ Pipe Cactus National Monument), and provide a rationale for the sample choice. When relevant, describe the organism taxa, source, sex, age range and any manipulations. State what population the sample is meant to represent when applicable. For studies involving existing datasets, describe the data and its source.*
Sampling strategy	*Note the sampling procedure. Describe the statistical methods that were used to predetermine sample size OR if no sample-size calculation was performed, describe how sample sizes were chosen and provide a rationale for why these sample sizes are sufficient.*
Data collection	*Describe the data collection procedure, including who recorded the data and how.*
Timing and spatial scale	*Indicate the start and stop dates of data collection, noting the frequency and periodicity of sampling and providing a rationale for these choices. If there is a gap between collection periods, state the dates for each sample cohort. Specify the spatial scale from which the data are taken*
Data exclusions	*If no data were excluded from the analyses, state so OR if data were excluded, describe the exclusions and the rationale behind them, indicating whether exclusion criteria were pre-established.*
Reproducibility	*Describe the measures taken to verify the reproducibility of experimental findings. For each experiment, note whether any attempts to repeat the experiment failed OR state that all attempts to repeat the experiment were successful.*
Randomization	*Describe how samples/organisms/participants were allocated into groups. If allocation was not random, describe how covariates were controlled. If this is not relevant to your study, explain why.*
Blinding	*Describe the extent of blinding used during data acquisition and analysis. If blinding was not possible, describe why OR explain why blinding was not relevant to your study.*

Did the study involve field work? ☐ Yes ☒ No

Reporting for specific materials, systems and methods

Materials & experimental systems

n/a	Involved in the study
☐	☐ Unique biological materials
☐	☒ Antibodies
☐	☒ Eukaryotic cell lines
☐	☐ Palaeontology
☐	☐ Animals and other organisms
☐	☐ Human research participants

Methods

n/a	Involved in the study
☐	☐ ChIP-seq
☐	☐ Flow cytometry
☐	☐ MRI-based neuroimaging

Unique biological materials

Policy information about availability of materials

Obtaining unique materials | *Describe any restrictions on the availability of unique materials OR confirm that all unique materials used are readily available from the authors or from standard commercial sources (and specify these sources).*

Antibodies

Antibodies used | Rabbit Anti NS1 and Mouse Anti NS2 , made in the P Roy's lab.

Validation

Describe the validation of each primary antibody for the species and application, noting any validation statements on the manufacturer's website, relevant citations, antibody profiles in online databases, or data provided in the manuscript.

Eukaryotic cell lines

Policy information about cell lines

Cell line source(s)

BSR Cells, Clone of BHK-21 obtained from ATCC

Authentication

Describe the authentication procedures for each cell line used OR declare that none of the cell lines used were authenticated.

Mycoplasma contamination

Negative for mycoplasma contamination (Tested by Hoechst staining)

Commonly misidentified lines
(See ICLAC register)

Name any commonly misidentified cell lines used in the study and provide a rationale for their use.

Palaeontology

Specimen provenance

Provide provenance information for specimens and describe permits that were obtained for the work (including the name of the issuing authority, the date of issue, and any identifying information).

Specimen deposition

Indicate where the specimens have been deposited to permit free access by other researchers.

Dating methods

If new dates are provided, describe how they were obtained (e.g. collection, storage, sample pretreatment and measurement), where they were obtained (i.e. lab name), the calibration program and the protocol for quality assurance OR state that no new dates are provided.

☐ Tick this box to confirm that the raw and calibrated dates are available in the paper or in Supplementary Information.

Animals and other organisms

Policy information about studies involving animals; ARRIVE guidelines recommended for reporting animal research

Laboratory animals

For laboratory animals, report species, strain, sex and age OR state that the study did not involve laboratory animals.

Wild animals

Provide details on animals observed in or captured in the field; report species, sex and age where possible. Describe how animals were caught and transported and what happened to captive animals after the study (if killed, explain why and describe method; if released, say where and when) OR state that the study did not involve wild animals.

Field-collected samples

For laboratory work with field-collected samples, describe all relevant parameters such as housing, maintenance, temperature, photoperiod and end-of-experiment protocol OR state that the study did not involve samples collected from the field.

Human research participants

Policy information about studies involving human research participants

Population characteristics

Describe the covariate-relevant population characteristics of the human research participants (e.g. age, gender, genotypic information, past and current diagnosis and treatment categories). If you filled out the behavioural & social sciences study design questions and have nothing to add here, write "See above."

Recruitment

Describe how participants were recruited. Outline any potential self-selection bias or other biases that may be present and how these are likely to impact results.

ChIP-seq

Data deposition

☐ Confirm that both raw and final processed data have been deposited in a public database such as GEO.

☐ Confirm that you have deposited or provided access to graph files (e.g. BED files) for the called peaks.

Data access links
May remain private before publication.

For "Initial submission" or "Revised version" documents, provide reviewer access links. For your "Final submission" document, provide a link to the deposited data.

Files in database submission

Provide a list of all files available in the database submission.

Genome browser session
(e.g. UCSC)

Provide a link to an anonymized genome browser session for "Initial submission" and "Revised version" documents only, to enable peer review. Write "no longer applicable" for "Final submission" documents.

Methodology

Replicates	*Describe the experimental replicates, specifying number, type and replicate agreement.*
Sequencing depth	*Describe the sequencing depth for each experiment, providing the total number of reads, uniquely mapped reads, length of reads and whether they were paired- or single-end.*
Antibodies	*Describe the antibodies used for the ChIP-seq experiments; as applicable, provide supplier name, catalog number, clone name, and lot number.*
Peak calling parameters	*Specify the command line program and parameters used for read mapping and peak calling, including the ChIP, control and index files used.*
Data quality	*Describe the methods used to ensure data quality in full detail, including how many peaks are at FDR 5% and above 5-fold enrichment.*
Software	*Describe the software used to collect and analyze the ChIP-seq data. For custom code that has been deposited into a community repository, provide accession details.*

Flow Cytometry

Plots

Confirm that:

☐ The axis labels state the marker and fluorochrome used (e.g. CD4-FITC).

☐ The axis scales are clearly visible. Include numbers along axes only for bottom left plot of group (a 'group' is an analysis of identical markers).

☐ All plots are contour plots with outliers or pseudocolor plots.

☐ A numerical value for number of cells or percentage (with statistics) is provided.

Methodology

Sample preparation	*Describe the sample preparation, detailing the biological source of the cells and any tissue processing steps used.*
Instrument	*Identify the instrument used for data collection, specifying make and model number.*
Software	*Describe the software used to collect and analyze the flow cytometry data. For custom code that has been deposited into a community repository, provide accession details.*
Cell population abundance	*Describe the abundance of the relevant cell populations within post-sort fractions, providing details on the purity of the samples and how it was determined.*
Gating strategy	*Describe the gating strategy used for all relevant experiments, specifying the preliminary FSC/SSC gates of the starting cell population, indicating where boundaries between "positive" and "negative" staining cell populations are defined.*

☐ Tick this box to confirm that a figure exemplifying the gating strategy is provided in the Supplementary Information.

Magnetic resonance imaging

Experimental design

Design type	*Indicate task or resting state; event-related or block design.*
Design specifications	*Specify the number of blocks, trials or experimental units per session and/or subject, and specify the length of each trial or block (if trials are blocked) and interval between trials.*
Behavioral performance measures	*State number and/or type of variables recorded (e.g. correct button press, response time) and what statistics were used to establish that the subjects were performing the task as expected (e.g. mean, range, and/or standard deviation across subjects).*

Acquisition

Imaging type(s)	*Specify: functional, structural, diffusion, perfusion.*
Field strength	*Specify in Tesla*
Sequence & imaging parameters	*Specify the pulse sequence type (gradient echo, spin echo, etc.), imaging type (EPI, spiral, etc.), field of view, matrix size, slice thickness, orientation and TE/TR/flip angle.*
Area of acquisition	*State whether a whole brain scan was used OR define the area of acquisition, describing how the region was determined.*

Diffusion MRI ☐ Used ☐ Not used

Preprocessing

Preprocessing software
Provide detail on software version and revision number and on specific parameters (model/functions, brain extraction, segmentation, smoothing kernel size, etc.).

Normalization
If data were normalized/standardized, describe the approach(es): specify linear or non-linear and define image types used for transformation OR indicate that data were not normalized and explain rationale for lack of normalization.

Normalization template
Describe the template used for normalization/transformation, specifying subject space or group standardized space (e.g. original Talairach, MNI305, ICBM152) OR indicate that the data were not normalized.

Noise and artifact removal
Describe your procedure(s) for artifact and structured noise removal, specifying motion parameters, tissue signals and physiological signals (heart rate, respiration).

Volume censoring
Define your software and/or method and criteria for volume censoring, and state the extent of such censoring.

Statistical modeling & inference

Model type and settings
Specify type (mass univariate, multivariate, RSA, predictive, etc.) and describe essential details of the model at the first and second levels (e.g. fixed, random or mixed effects; drift or auto-correlation).

Effect(s) tested
Define precise effect in terms of the task or stimulus conditions instead of psychological concepts and indicate whether ANOVA or factorial designs were used.

Specify type of analysis: ☐ Whole brain ☐ ROI-based ☐ Both

Statistic type for inference
(See Eklund et al. 2016)
Specify voxel-wise or cluster-wise and report all relevant parameters for cluster-wise methods.

Correction
Describe the type of correction and how it is obtained for multiple comparisons (e.g. FWE, FDR, permutation or Monte Carlo).

Models & analysis

n/a	Involved in the study
☐	☐ Functional and/or effective connectivity
☐	☐ Graph analysis
☐	☐ Multivariate modeling or predictive analysis

Functional and/or effective connectivity
Report the measures of dependence used and the model details (e.g. Pearson correlation, partial correlation, mutual information).

Graph analysis
Report the dependent variable and connectivity measure, specifying weighted graph or binarized graph, subject- or group-level, and the global and/or node summaries used (e.g. clustering coefficient, efficiency, etc.).

Multivariate modeling and predictive analysis
Specify independent variables, features extraction and dimension reduction, model, training and evaluation metrics.